Interferometric Image Reconstruction with Compressed Sensing and Stockwell Transform

Yu-Hsuan Teng *(wendydern1@gmail.com)*
Advisor: Prof. Jean-Fu Kiang
National Taiwan University (NTU)

***Abstract*—With the high sensitivity and angular resolution of next-generation radio telescopes such as the Square Kilometre Array (SKA), high time-resolution universe at radio wavelengths can be revealed. We simulate the instantaneous visibility data of M31 based on possible SKA configuration, and performed reconstruction by implementing state-of-the-art algorithms such as CLEAN, MS-CLEAN and IUWT-based compressed sensing (CS) method. It has been proved that the IUWT-based CS method outperforms the CLEAN-based algorithms. Furthermore, we show the potential of the discrete orthogonal Stockwell transform (DOST), which can reveal more details than the IUWT. Therefore, we propose to associate the compressed sensing technique with the Stockwell transform for a better optimization of the reconstruction in radio interferometric imaging.**

I. Introduction

A radio interferometer assembles an array of radio telescopes that work together as a large single telescope to achieve higher resolution. Unlike single dish telescopes, radio interferometers provide discretely-sampled visibility, which is a cross-power spectrum in spatial frequency (u, v). Hence, one critical challenge in radio interferometry is to reconstruct the intensity of astronomical sources from such discretely-sampled visibility. This is known as the interferometric inverse problem.

Aimed at improving the reconstruction of astronomical signals from interferometers, state-of-the-art approaches include CLEAN, Multi-scale CLEAN, and compressive-sensing (CS)-based methods. In general, astronomical signals can be categorized into point sources or extended sources. Therefore, it is reasonable to assume sparsity of astronomical image in either image or wavelet domain.

To reconstruct astronomical images by using wavelet basis in CS, an isotropic undecimated wavelet transform (IUWT)-based CS method was proposed in [1], where the linear imaging system can be represented as

$$\bar{V} = \bar{\bar{\Phi}} \cdot \bar{I} = \bar{\bar{\Phi}} \cdot \bar{\bar{\Psi}} \cdot \bar{\alpha} \tag{1}$$

where $\bar{V}$ is the observed visibility vector, $\bar{\bar{\Phi}}$ is the matrix representing two-dimensional Fourier transform and sampling in the uv domain, and $\bar{I}$ is the reconstructed image which has a sparse representation $\bar{\alpha}$, and IUWT-based dictionary $\bar{\bar{\Psi}}$. Then, the image can be reconstructed by solving

$$\bar{I} = \arg\min_{\bar{I}} \left\{ \|\bar{V} - \bar{\bar{\Phi}} \cdot \bar{I}\|_2 + \tau \|\bar{\alpha}\|_1 \right\}$$

where τ is the regularization parameter.

However, high time-resolution universe at radio wavelengths remain unexplored because the sampling rate is low due to insufficient sensitivity of most radio telescopes. To increase sensitivity, most existing fast radio transients are detected with large aperture single dish telescopes. However, the localization of transient signals performs poorly due to the limited angular resolution of single dish telescopes.

Requirments for fast radio transients detection include high instantaneous sensitivity, large field-of-view (FoV), capability of localizing the source of an emission with high angular resolution [4], [5]. Therefore, next-generation radio interferometer arrays, such as the Squared Kilometre Array (SKA), is designed with large number of radio telescopes and small elements / dishes to reach those requirements.

Two major goals of SKA is to observe transient sources and 21 cm hydrogen line in galaxies. With the increased sensitivity and field of view of the SKA, more extragalactic or fainter transient soucres can be detected to test the theoretical mechanisms of compact, high-energy objects such as neutron stars or black holes. The unrival sensitivity and resolution of the SKA in the 21 cm hydrogen line (1,420 MHz) will also be able to reveal young, newly formed galaxies at cosmological distances, which helps unravel the processes of galaxy formation and evolution.

In this work, we plan to simulate galaxies observed with SKA, and then compare our recontruction methods with state-of-the-art algorithms such as CLEAN, Multi-scale CLEAN, and IUWT-based CS methods. The reconstruction approach proposed is based on the basis pursuit denoise (BPDN) in CS, with a 2-D decomposition by the Stockwell transform. The major contribution of this work is the introduction of Stockwell transform into interferometric image reconstruction. With the high sensitivity and angular resolution of next-generation radio telescopes such as the SKA, our proposed method aims at detailed reconstruction with high time-resolution.

II. Reconstruction Theory and Algorithms

The intensity $I(x, y)$ of an astronomical source and the visibility $V(u, v)$ are a two-dimensional Fourier transform pair, which can be formulated as [1]

$$V(u, v) = \iint I(x, y) e^{-2\pi i(ux+vy)} dxdy \tag{2}$$

$$I(x, y) = \iint V(u, v) e^{2\pi i(ux+vy)} dudv \tag{3}$$

where (x, y) represents the sky coordinates in units of radian, and (u, v) are defined as $u = U/\lambda$ and $v = V/\lambda$, where U

and V are the physical lengths of the projected baseline and λ is the observed wavelengh.

Due to the wide spacing between antennas, there are many unsampled data points in the uv plane. The limited uv coverage problem is usually solved by filling unsampled visibilities with zero [2], which is known as zero-padding technique. In this way, (3) can be rewritten as

$$I^D(x,y) = \iint V(u,v)S(u,v)e^{-2\pi i(ux+vy)}dudv \quad (4)$$

where $S(u,v)$ represents the sampling mask of $V(u,v)$. The resulting I^D is called the dirty image. Such reconstructed image obtained by (4) is known to cause numerous ripples and a finite resolution-cell size in the resultant images [2].

Angular resolution, which is often referred to as diffraction limit and beam size in optical and radio astronomy, respectively, is given by

$$\theta \simeq \frac{\lambda}{D}$$

where λ is the observing wavelength and D is the diameter of a single dish telescope or the maximum baseline of an interferometer array. Objects with angular distance smaller than the angular resolution θ can not be resolved due to limited diameter or baseline.

Although longer baselines in interferometry can result in a higher resolution, extended structure, which has wider and smoother emission, can only be reconstructed by observation with shorter baselines. However, the minimal baselines are limited by the dish sizes in practice.

The CLEAN algorithm is the most successful and widely-used method for deconvolving interferometric data [8]. By assuming that the observed emission is only composed of point sources, the CLEAN algorithm iteratively finds the highest peak in the residual map, subtracts a beam-convolved fraction of a delta function fitted to the peak, and saves the δ components in a separate image.

To improve the quality of CLEAN algorithm in reconstructing extended sources, the Multi-Scale CLEAN (MS-CLEAN) was proposed [9]. Unlike traditional CLEAN algorithm using Dirac-delta functions, MS-CLEAN uses components in different scales to model astronomical sources. Multi-Scale CLEAN is stable in the presence of a spatially varying background provided sufficiently large scales are included in the search. The large scale structure is removed first, and then the fine scale structure is left to be estimated on a largely empty background.

Very recent approaches using compressive sensing (CS) with sparse modeling provide an additional constraint which assumes sparsity of the image. It can be used in resolving compact sources such as the super-resolution image of black hole shadow or point sources. Even if the assumption of sparsity in the image domain would no longer hold for extended sources, we can also transform our image to another domain in which the corresponding solution becomes sparse, for example, the wavelet domain.

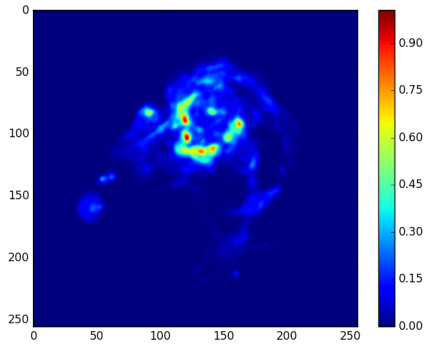

Fig. 1. M31 test image used in radio astronomy simulations [9], [12], [14].

III. Simulation of the SKA Data

A. Test Image and SKA Configuration

Fig.1 shows the intensity distribution (256×256 pixels) of an M31 test image at declination of $35°$, which is taken at 1.42 GHz. The maximum intensity is normalized to 1.

The configuration of the SKA compact array proposed in [22] contains 1,200 antennas within an area of diameter less than 3 km and approximately 2320 antennas inside 35 km. As a precursor of the mid-band SKA, the antennas of the MeerKAT array are distributed in a two-dimensional fashion with a Gaussian uv-distribution [23]. By assuming two different 2-D Gaussian distribution within 3 km and 35 km, respectively, we simulate the SKA compact array that fits the conditions proposed in [22].

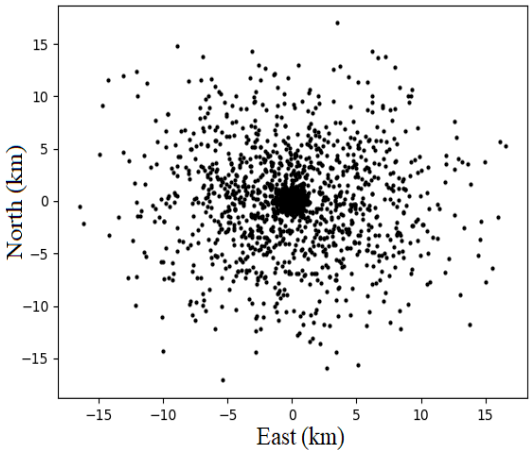

Fig. 2. Simulated locations of the antennas in the central 35 km core of SKA [22], with the center assumed at latitude 34°N.

Fig.2 shows the simulated locations of the antennas in the central 35 km core of SKA, with the center assumed at latitude 34°N.

For a target with hour angle h and declination δ, the relation between the baseline vector $\bar{B}$ and the sampled spatial frequencies can be represented as [16]

$$\begin{bmatrix} U \\ V \\ W \end{bmatrix} = \frac{1}{\lambda} \begin{bmatrix} \sin h & \cos h & 0 \\ -\sin\delta\cos h & \sin\delta\sin h & \cos\delta \\ \cos\delta\cos h & -\cos\delta\sin h & \sin\delta \end{bmatrix} \begin{bmatrix} \Delta X \\ \Delta Y \\ \Delta Z \end{bmatrix} \quad (5)$$

B. Visibility Data Simulation

The uv coverage of an interferometer array is represented by the projected baseline vector on the sky, which depends on the declination and the hour angle of the source. The baseline vector $\bar{B}$, which implies the difference of coordinates between the telescopes, is represented as

$$\bar{B} = \Delta X\bar{i} + \Delta Y\bar{j} + \Delta Z\bar{k}$$

where $\bar{i}$, $\bar{j}$ and $\bar{k}$ point respectively toward the East, the North and the Meridian.

By using the coordinates of the antennas in Fig.2, the uv coverage for the M31 test image, which is at declination $35°$, can be simulated by substituting Δx, Δy and Δz of each baseline pair into (5). Fig. 3 shows the instantaneous uv coverage of the simulated central core of the SKA, assumed to observe the M31 test image at declination $35°$.

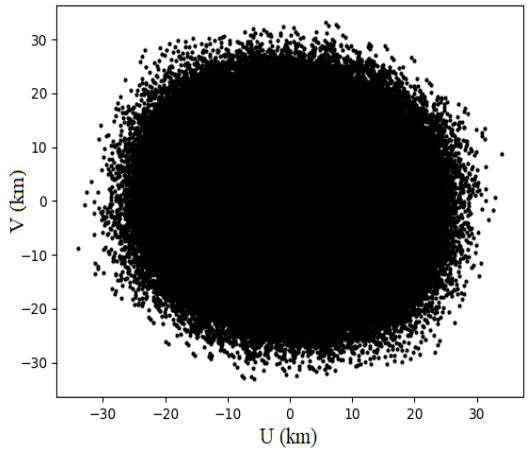

Fig. 3. Simulated instantaneous uv coverage of the simulated central core of the SKA, assumed to observe the M31 test image at declination $35°$.

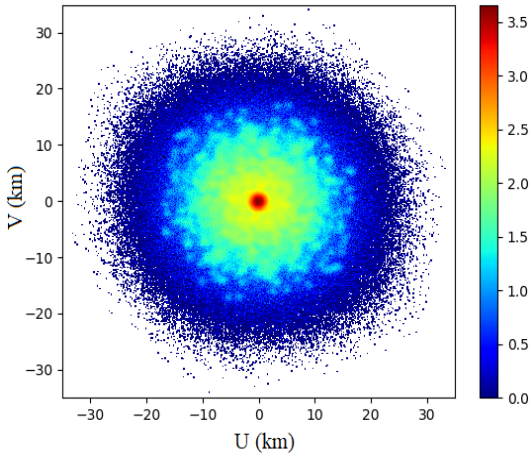

Fig. 4. Number density (in log scale) of the simulated configuration of SKA in Fig.2, with 100 m^2 per cell.

Fig.4 shows the number density of the simulated configuration of SKA. The number density is defined as the number of visibility data in each cell.

To simulate the observed visibility data at each point on the uv coverage plane, the Fourier relation in (2) and (3) are applied to the test image to obtain the complex visibilities of those points as

$$V(u,v) = \Delta x \Delta y \sum_{x=-M/2}^{M/2-1} \sum_{y=-N/2}^{N/2-1} I[x,y] e^{-2\pi i(ux\Delta x + vy\Delta y)} \tag{6}$$

where M and N are the number of pixels along the x and y direction, Δx and Δy are the angular resolution of each pixel in radians, and u, v are the baselines represented by the observed wavelength λ.

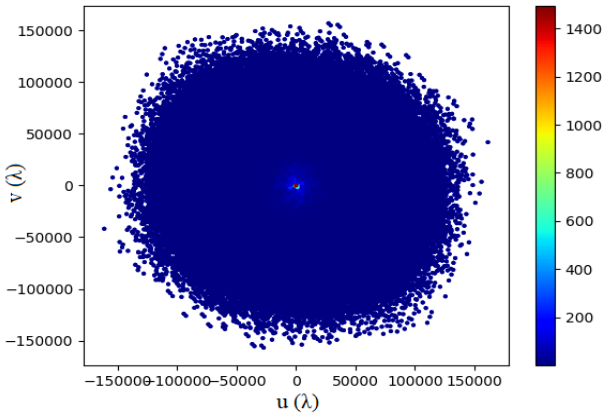

Fig. 5. Simulated visibility data of the central $35km$ core of the SKA.

Fig.5 shows the simulated visibility data of the $35km$ central core of the SKA.

C. Dirty image Reconstruction

We regrid the simulated visibility data obtained from (6) by the triangulation-based linear barycentric interpolation method [18]. In the triangulation-based linear barycentric interpolation method, the regridded data at a grid point can be represented as the weighted average of the values at the three vertices of the enclosing triangle as

$$V = \lambda_1 V_1 + \lambda_2 V_2 + \lambda_3 V_3$$

where $\lambda_1 + \lambda_2 + \lambda_3 = 1$, and V_1, V_2 and V_3 are the measured visibility data at the three vertices.

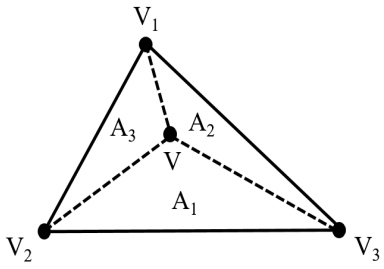

Fig. 6. Illustration of the triangulation-based barycentric linear interpolation [18].

Fig.6 illustrates the triangulation-based barycentric linear interpolation. λ_α are defined as the percentage of each corresponding area, namely, $\lambda_\alpha = A_\alpha / \sum_{k=1}^{3} A_k$.

With the regridded visibility, the dirty image can be reconstructed as

$$I^D[x,y] = \Delta u \Delta v \sum_{u=-M/2}^{M/2-1} \sum_{v=-N/2}^{N/2-1} V[u,v] e^{2\pi i(u\Delta u x \Delta x + v \Delta v y \Delta y)} \tag{7}$$

where Δu and Δv are the spacing of each regridded visibility cell in radians. In Python, the 2-D inverse FFT is defined as

$$\begin{aligned} I[x,y] &= \frac{1}{MN} \sum_{u=0}^{M-1} \sum_{v=0}^{N-1} V[u,v] e^{2\pi i(u\Delta u_0 x \Delta x + v \Delta v_0 y \Delta y)} \\ &= \frac{1}{MN} \sum_{u=0}^{M-1} \sum_{v=0}^{N-1} V[u,v] e^{2\pi i(ux/M + vy/N)} \end{aligned} \tag{8}$$

where $1/M = \Delta u_0 \Delta x$ and $1/N = \Delta v_0 \Delta x$ due to the uncertainty principle.

If we assume $M = N$ in (7) and (8), the relation between the dirty image and the inverse FFT can be derived as

$$\begin{aligned} I^D[x,y] &= \frac{1}{\Delta x \Delta y} \sum_{u=-N/2}^{N/2-1} \sum_{v=-N/2}^{N/2-1} \\ &\quad V[u,v] e^{2\pi i(u\Delta u_0 u' x \Delta x + v \Delta v_0 v' y \Delta y)} \\ &= \frac{1}{\Delta x \Delta y} \sum_{u=-N/2}^{N/2-1} \sum_{v=-N/2}^{N/2-1} V[u,v] e^{2\pi i(uu'x + vv'y)/N} \end{aligned}$$

where $u' = \Delta u / \Delta u_0$ and $v' = \Delta v / \Delta v_0$ are the scaling factors along the u and v directions.

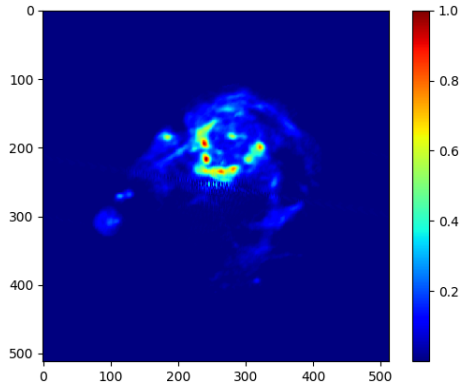

Fig. 7. Dirty image with 512×512 pixels obtained from the simulated instantaneous visibility data of the SKA.

Fig.7 shows the dirty image with 512×512 pixels obtained from the simulated instantaneous visibility data of the SKA, by directly applying inverse FFT to the regridded visibility data.

The synthesized beam caused by the sampling holes on uv plane is defined as

$$B = \mathcal{F}^{-1}\{S\} \tag{9}$$

where S is the sampling mask on uv plane, with $S(u,v) = 1$ for all measured data points and $S(u,v) = 0$ otherwise. Similar to the procedure of obtaining the dirty image, we derive the regridded sampling mask via the triangulation-based linear barycentric interpolation, and then apply two-dimensional inverse Fourier transform to obtain the synthesized beam.

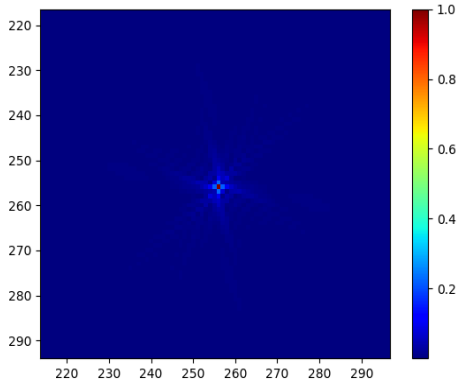

Fig. 8. Synthesized beam of the simulated SKA observation on M31 test image.

Fig.8 shows the synthesized beam of the simulated observation on M31.

IV. Reconsruction Algorithm

A. Compressive Sensing (CS) Based Reconstruction

Theoretically, CS uses basis pursuit (BP) approach to find the solution to (1) by solving

$$\min \|\bar{\alpha}\|_1 \qquad s.t. \quad \bar{V} = \bar{\bar{S}} \cdot \bar{\bar{F}} \cdot \bar{\bar{W}}^{-1} \cdot \bar{\alpha} \tag{10}$$

In practice, for measurements contaminated by noises, BP can be replaced by a more general algorithm: basis pursuit denoise (BPDN), where the solution is given by

$$\min \|\bar{\alpha}\|_1 \qquad s.t. \quad \|\bar{V} - \bar{\bar{S}} \cdot \bar{\bar{F}} \cdot \bar{\bar{W}}^{-1} \cdot \bar{\alpha}\|_2 \leq \varepsilon \tag{11}$$

With the IUWT basis, the equation of image reconsruction via compressive sensing in (1) can be rewritten as

$$\bar{\alpha} = \arg\min_{\bar{\alpha}} \left\{ \|\bar{V} - \bar{\bar{S}} \cdot \bar{\bar{F}} \cdot \bar{\bar{W}}^{-1} \cdot \bar{\alpha}\|_2 + \lambda \|\bar{\alpha}\|_1 \right\} \tag{12}$$

where $\bar{\bar{S}}$ is the sampling mask of uv domain, $\bar{\bar{F}}$ is the 2D Fourier matrix, and $\bar{\bar{W}}^{-1}$ is the inverse IUWT. Since astronomical images contain mostly isotropic or quasi-isotropic objects such as stars, galaxies or galaxy clusters, the IUWT is the most popular wavelet transform algorithm in astronomy [11].

In IUWT, an $N \times N$ image c_0 is decomposed into a coefficient set $W = \{w_1, ..., w_S, c_S\}$ as [10]

$$c_0[m,n] = c_S[m,n] + \sum_{s=1}^{S} w_s[m,n]$$

where c_S is a coarse or smooth version of the original image c_0 and w_s represents the details of c0 at scale 2^{-s}. The index $s = 1$ corresponds to the finest scale or highest frequency

structure. The passage from one resolution to the next one is obtained as

$$c_{s+1}[m,n] = \sum_{k=1}^{K}\sum_{\ell=1}^{L} h_{1D}[k]h_{1D}[\ell]c_s[m+2^s k, n+2^s \ell] \quad (13)$$

$$w_{s+1}[m,n] = c_s[m,n] - c_{s+1}[m,n] \quad (14)$$

where h_{1D} is typically a symmetric low-pass filter. In IUWT, the non-orthogonal Astro filter bank is used as

$$h_{1D} = \{1,4,6,4,1\}/16 \quad (15)$$

and the corresponding high-pass filter is

$$g_{1D} = \{-1,-4,10,-4,-1\}/16$$

However, the high-pass filter is redundant in IUWT, since the high frequency image can be recontructed by the subtraction of the current-stage low frequency image with the previous-stage low frequency image, as formulated by (14).

B. Discrete Orthogonal Stockwell Transform (DOST)

The 2-D Stockwell transform (ST) with a Gaussian window for a continuous-domain function $h(x',y')$ is defined as [19]

$$S(x,y,u,v) = \int_{-\infty}^{\infty}\int_{-\infty}^{\infty} h(x',y')\frac{uv}{2\pi}e^{-[(x'-x)^2u^2+(y'-y)^2v^2]/2} e^{-i2\pi(ux'+vy')}dx'dy' \quad (16)$$

Thus, the shape of the Gaussian kernel changes with respect to spatial frequencies u and v.

The 2-D ST has a close relation to the Fourier transform (FT), which can be written as

$$H(u,v) = \int_{-\infty}^{\infty}\int_{-\infty}^{\infty} S(x,y,u,v)dxdy \quad (17)$$

where $H(u,v) = \mathcal{F}\{h(x',y')\}$. Through the relation with FT, the ST in (16) can also be represented as operations on the Fourier spectrum $H(\alpha,\beta)$

$$S(x,y,u,v) = \int_{-\infty}^{\infty}\int_{-\infty}^{\infty} H(\alpha+u,\beta+v)e^{-2\pi^2\alpha^2/u^2}e^{-2\pi^2\beta^2/v^2} e^{i2\pi(\alpha x+\beta y)}d\alpha d\beta$$

Taking advantage of the FFT calculation, the discrete 2-D ST coefficients of an image $h[m,n]$ can be expressed as

$$S[m,n,u,v] = \sum_{\alpha=0}^{M-1}\sum_{\beta=0}^{N-1} H[\alpha+u,\beta+v]e^{-2\pi^2\alpha^2/u^2}e^{i2\pi\alpha m/M} e^{-2\pi^2\beta^2/v^2}e^{i2\pi\beta n/N}\Delta\alpha\Delta\beta$$

where $m = 0,1,...,M-1$ and $n = 0,1,...,N-1$. The relation between ST and FT in (17) can be discretized as

$$H[u,v] = \frac{1}{N}\sum_{n=0}^{N-1}\frac{1}{M}\sum_{m=0}^{M-1} S[m,n,u,v]$$

where $H[u,v]$ are the discrete 2-D Fourier coefficients. Therefore, the original image can be reconstructed as

$$h[m,n] = \left(\frac{1}{N}\right)^2\sum_{n'=0}^{N-1}\sum_{v=0}^{N-1}\left(\frac{1}{M}\right)^2\sum_{m'=0}^{M-1}\sum_{u=0}^{M-1} S[m',n',u,v]e^{i2\pi\alpha m/M}e^{i2\pi\beta n/N}\Delta u\Delta v$$

Based on the sampling theorem, less spatial resolution is required for a lower frequency band. Therefore, the discrete orthogonal Stockwell transfrom (DOST) was proposed to reduce the storage and speed up the discrete Stockwell transform by pursuing a non-overlapping multi-resolution partition over the time-frequency domain [20].

V. Implementation Results and Discussions

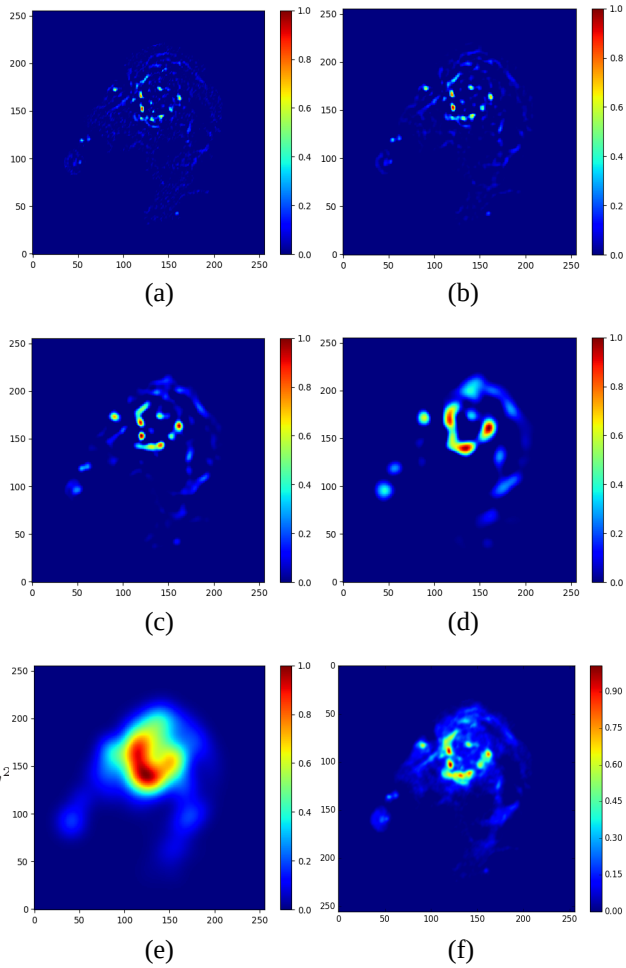

Fig. 9. IUWT of M31 up to 4 scales. The maximum intensity of each image is normalized to 1. (a)-(e) Four wavelet scales and the final low frequency image by performing IUWT of the M31 test image, (f) original M31 test image.

We composed a multi-stage IUWT Python code and demonstrate on the test image. Fig. 9 shows the results of four-stage IUWT of the simulated M31. Fig. 9(a) to (e) represent the images from the highest frequency to the lowest frequency, corresponding to the wavelet coefficeients $w_1, w_2, ..., w_4, c_4$, respectively.

Consider an $M \times N$ image with s-stage IUWT decomposition and $M \times N$ points on the uv plane. Then, we have $\bar{\alpha}$ with length $(s+1)MN$, $\bar{\bar{W}}^{-1}$ with size $MN \times (s+1)MN$, and $\bar{\bar{S}}\bar{\bar{F}}$ with size $MN \times MN$. The DFT matrix can be generated

as

$$\bar{\bar{F}} = \begin{bmatrix} 1 & 1 & 1 & \cdots & 1 \\ 1 & \omega & \omega^2 & \cdots & \omega^{MN-1} \\ 1 & \omega^2 & \omega^4 & \cdots & \omega^{2(MN-1)} \\ \vdots & \vdots & \vdots & \ddots & \vdots \\ 1 & \omega^{MN-1} & \omega^{2(MN-1)} & \cdots & \omega^{(MN-1)(MN-1)} \end{bmatrix}$$

where $\omega = e^{-i2\pi/MN}$.

Limited by our computer memory, we take $M = N = 65$ and $s = 4$ with the simulated visibility data of the SKA. Thus, we regrid the uv plane with $104 \times 104m^2$ per grid so that we have 65×65 points on our uv plane. After solving the equation with BPDN, the reconstructed $\bar{\alpha}$ is obtained. We then apply inverse IUWT on $\bar{\alpha}$ to solve the reconstructed image.

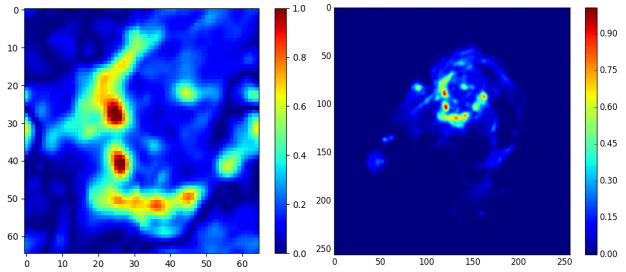

(a) (b)

Fig. 10. (a) Reconstructed M31 test image (256×256) with size 65×65 by using BPDN with $\varepsilon = 0.001$. (b) Original M31 test image (256×256) for comparison.

The results using BPDN with $\varepsilon = 0.001$ are shown in Fig. 10(a), with residuals at the order of 10^{-4}. Since we assumed a 65×65 image instead of a 256×256 image due to memory issues, the reconstructed image only shows the brightest central part of M31, recovering $\sim 56\%$ flux of the original 256×256 image.

We propose a reconstruction algorithm using DOST-based CS for 2D image reconstruction. Unlike the wavelet basis functions, DOST basis are not self-similar. In wavelet transforms, a phase modulation is applied to the frequency domain due to the shift of wavelet functions in space. But the basis functions of the DOST are not shifted and not self-similar to each other. Furthermore, since DOST has a direct relation to DFT, the absolutely-referenced frequency and phase information can be maintained if applying DOST.

Define the mean square error (MSE) of a reconstructed signal $x(t)$ with size N as

$$MSE = \frac{1}{N} \sum_{n=0}^{N-1} [x(t) - k(t)]^2 \tag{18}$$

where $k(t)$ is the reference or the original input signal. Then, the peak signal to noise ratio (PSNR) of x is defined as

$$PSNR = 20 \log \frac{x_{\max}}{\sqrt{MSE}} \tag{19}$$

We derive both IUWT and DOST coefficients on the of the M31 test image, respectively, and then compare the reconstructed M31 images after compressing the smallest 90% of those coefficients to zeros. Fig.11 shows both the compressed IUWT and compressed DOST coefficients of the M31 test image.

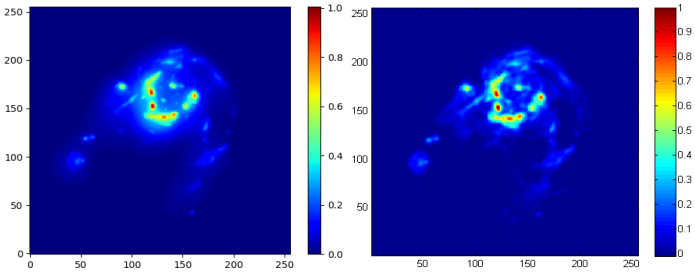

(a) (b)

Fig. 11. Reconstructed M31 images using 10% of coefficients. (a) IUWT-reconstructed image with $MSE = 4.6 \times 10^{-4}$ and $PSNR = 33.38$, (b) DOST-reconstructed image with $MSE = 4.5 \times 10^{-6}$ and $PSNR = 53.46$.

The IUWT-reconstructed and DOST-reconstructed M31 images are shown in Fig.11 (a) and (b), with $MSE = 4.6 \times 10^{-4}$, $PSNR = 33.38$ and $MSE = 4.5 \times 10^{-6}$, $PSNR = 53.46$, respectively.

As one can see, the DOST-reconstructed M31 remains sharper and more detailed information than the IUWT-reconstucted M31. In the region with more extended emssion, it is clear that the DOST-reconstructed M31 also keep more original texture than the IUWT-reconstucted M31.

Finally, we compare the reconstruction with the most widely-used algorithms: CLEAN [8] and MS-CLEAN [9]. On the basis of the two original papers ([8] and [9]), we construct our own Python codes for CLEAN and MS-CLEAN. Reconstruction of the M31 image with these two methods are demonstrated in Fig.12.

Since the CLEAN algorithm assumes sparsity in image domain, it requires huge number of iterations to represent an extended source completely, which not only increases the computation time but also creates negative bowls around the emission. The results applied on the dirty image of M31 with

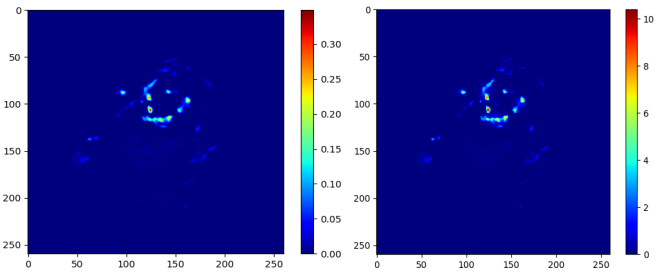

(a) (b)

Fig. 12. (a) CLEAN [8] reconstructed image with 15000 iterations and a loop gain of 0.1. (b) MS-CLEAN [9] reconstructed image with 15,000 iterations, a loop gain of 1, and scale parameters of $\alpha = 0, 3, 6, 12, 24$ pixels.

15000 iterations and a loop gain of 0.1 are shown in Fig. 12(a). Fig. 12(b) shows the final model image of MS-CLEAN with a loop gain of 1, applied on the M31 dirty image with scale parameters $\alpha = 0, 3, 6, 12, 24$ pixels.

The CLEAN and MS-CLEAN algorithms implicitly assume the sparsity of astronomical images in the Dirac space and the wavelet space, respectively, and solve them by matching pursuit (MP) procedure. IUWT-based algorithms assume sparsity of astronomical images through IUWT bases, and solve the minimization problem by basis pursuit (BP) related approaches such as BPDN.

In this paper, all the mentioned state-of-the-art algorithms have been implemented and discussed. In addition, we demonstrated that the Stockwell transform (DOST) is even more effective in reconstructing the details of astronomical image than the wavelet transform (IUWT). Therefore, we believe that DOST-based CS method has a great potential in the improvement of radio interferometric image reconstruction.

REFERENCES

[1] F. Li, T. Cornwell and F. de Hoog, "The application of compressive sampling to radio astronomy I. Deconvolution," *Astronomy and Astrophysics*, vol. 528, Apr. 2011.

[2] M. Honma, K. Akiyama, M. Uemura and S. Ikeda, "Super-resolution imaging with radio interferometry using sparse modeling," *Publications of the Astronomical Society of Japan*, vol. 66, no. 5, Sep. 2014.

[3] D. Frail, "Transients, fast and slow," 14th Synthesis Imaging Workshop, National Radio Astronomy Observatory, Socorro New Mexico, May 2014.

[4] M. Obrocka, B. Stappers and P. Wilkinson, "Localising fast radio bursts and other transients using interferometric arrays," *Astronomy and Astrophysics*, vol. 579, Jul. 2015.

[5] N. Clarke, L. D'Addario, R. Navarro and J. Trinh, "A Multi-Beam Radio Transient Detector With Real-Time De-Dispersion Over a Wide DM Range," *Journal of Astronomical Instrumentation*, vol. 3, no.1, Mar. 2014.

[6] R. Khan, "Spitzer photometry of $\sim$1 million stars in M31 and 15 other galaxies," *The Astrophysical Journal Supplement Series*, vol. 228, no.1, Jan. 2017.

[7] M. Jiang *et al*., "Compressed sensing and radio interferometry," *European Signal Processing Conference*, Sep. 2015.

[8] J. Hogbom, "Aperture Synthesis with a Non-Regular Distribution of Interferometer Baselines," *Astronomy and Astrophysics Supplement*, vol. 15, p. 147, Jun. 1974.

[9] T. Cornwell, "Multiscale CLEAN Deconvolution of Radio Synthesis Images," *IEEE Journal of Selected Topics in Signal Processing*, vol. 2, Iss. 5, Oct. 2008.

[10] J. Starck, J. Fadili and F. Murtagh "The Undecimated Wavelet Decomposition and its Reconstruction," *IEEE Transactions on Image Processing*, vol. 16, no. 2, Feb. 2007.

[11] J. Starck and J. Bobin, "Astronomical data analysis and sparsity: From wavelets to compressed sensing," *Proceedings of the IEEE*, vol. 98, Iss. 6, Oct. 2009.

[12] R. Carrillo, J. McEwen and Y. Wiaux, "Sparsity Averaging Reweighted Analysis (SARA): a novel algorithm for radio-interferometric imaging," *Monthly Notices of the Royal Astronomical Society*, vol. 426, Iss. 2, Oct. 2012.

[13] A. Beck and M. Teboulle, "A Fast Iterative Shrinkage-Thresholding Algorithm for Linear Inverse Problems," *SIAM Journal on Imaging Sciences*, vol. 2, no.1, Mar. 2009.

[14] A. Dabbech *et al*., "MORESANE: MOdel REconstruction by Synthesis-ANalysis Estimators," *Astronomy and Astrophysics*, vol. 576, Mar. 2015.

[15] J. McMullin *et al*., "CASA Architecture and Applications," *Astronomical Data Analysis Software and Systems XVI ASP Conference Series*, vol. 376, Oct. 2007.

[16] D. Segransan, "Observability and UV coverage," *New Astronomy Reviews*, vol. 51, Oct. 2007.

[17] https://en.wikipedia.org/wiki/Delaunay_triangulation

[18] K. Hormann, "Barycentric Interpolation," *Springer Proceedings in Mathematics and Statistics*, vol. 83, 2014.

[19] Y. Wang, "Efficient Stockwell Transform with Applications to Image Processing," PhD Thesis, University of Waterloo, Ontario Canada, 2011.

[20] R. Stockwell, "A basis for efficient representation of the S-transform," *Digital Signal Processing*, vol. 17, Jan. 2007.

[21] Y. Wang and J. Orchard, "Fast Discrete Orthonormal Stockwell Transform," *SIAM Journal on Scientific Computing*, vol. 31, Nov. 2009.

[22] U.S. Square-Kilometer Array Consortium, "The Square Kilometer Array, Preliminary Strawman Design Large NVSmall D," *SKA Memo 18*, July 2002.

[23] W. de Blok, "The MeerKAT Karoo Array Telescope and its HI Emission Line Surveys," *Proceedings of the International Astronomical Union*, vol. 6, Dec. 2010.

[24] V. Ravi and P. Lasky "The birth of black holes: neutron star collapse times, gamma-ray bursts and fast radio bursts," *Monthly Notices of the Royal Astronomical Society*, vol. 441, Apr. 2014.

[25] B. Zhang, "A possible connection between fast radio bursts and gamma ray bursts," *The Astrophysical Journal Letters*, vol. 780, no. 2, Dec. 2013.

[26] B. Metzger1 and E. Berger, "What is the most promising electromagnetic counterpart of a neutron star binary merger," *The Astrophysical Journal*, vol. 746, no. 1, Jan. 2012.

[27] P. Scholz *et al*., "The repeating fast radio burst FRB 121102: multi-wavelength observations and additional bursts," *The Astrophysical Journal*, vol. 833, Dec. 2016.

[28] K. Masui *et al*., "Dense magnetized plasma associated with a fast radio burst," *Nature*, vol. 528, Dec. 2015.

[29] N. Tanvir *et al*., "A kilonova associated with the short-duration gamma ray burst GRB 130603B," *Nature*, vol. 500, Aug. 2013.